

# Scaling laws in spherical shell dynamos with free-slip boundaries

Rakesh K. Yadav, Thomas Gastine, Ulrich R. Christensen

*Max-Planck-Institute für Sonensystemforschung, 37191, Katlenburg-Lindau, Germany*

## Abstract

Numerical simulations of convection driven rotating spherical shell dynamos have often been performed with rigid boundary conditions, as is appropriate for the metallic cores of terrestrial planets. Free-slip boundaries are more appropriate for dynamos in other astrophysical objects, such as gas-giants or stars. Using a set of 57 direct numerical simulations, we investigate the effect of free-slip boundary conditions on the scaling properties of heat flow, flow velocity and magnetic field strength and compare it with earlier results for rigid boundaries. We find that the nature of the mechanical boundary condition has only a minor influence on the scaling laws. We also find that although dipolar and multipolar dynamos exhibit approximately the same scaling exponents, there is an offset in the scaling pre-factors for velocity and magnetic field strength. We argue that the offset can be attributed to the differences in the zonal flow contribution between dipolar and multipolar dynamos.

## 1. Introduction

Numerical simulations of dynamos in geometries appropriate for the cores of terrestrial planets have greatly enhanced our understanding of the complex magnetic field behavior observed in these objects, with possible implications for a broader class of dynamos in astrophysical objects (Jones, 2011). One of the major drawbacks of such simulations is that there is order of magnitude disagreement between the natural and the numerically accessible values of several control parameters. For instance, in numerical simulations of the geodynamo, the Ekman number – a nondimensional measure of the importance of viscous effects as compared to the Coriolis effects – is usually five to ten orders of magnitude larger than the expected realistic values.

One way to tackle this disparity is to infer asymptotic scaling laws from a sufficient number of numerical results. Such numerical scaling laws can then be extrapolated to realistic parameter regimes and compared with the observational data. Christensen and Aubert (2006) (hereafter “CA6”) used a battery of numerical simulation results to derive scaling relations for heat transfer, convective velocity, and magnetic field strength. Their scaling relations hold over several orders of magnitude of the relevant control parameter. Using these scaling relations, CA6 predicted magnetic field strengths inside the Earth’s and Jupiter’s core and found reasonable agreement with observationally constrained values. Later, Christensen et al. (2009) showed that these scaling laws are also in good agreement with magnetic fields observed in fast rotating low-mass stars. Takahashi et al. (2008) and Aubert et al. (2009) independently re-enforced the scaling laws put forth by CA6. Olson and Christensen (2006) derived scaling laws specifically for the dipole moment of planetary dynamos which show an

order-of-magnitude agreement with the observed dipole moments of solar system planets. Christensen (2010) reviews earlier scaling laws for planetary magnetic field based on heuristic arguments and compares them with the numerically established scaling relations.

The mechanical boundary conditions may play an important role in the dynamo mechanism. Dynamos which operate in planets with a solid mantle are usually modeled with rigid boundaries (Kageyama and Sato, 1995; Glatzmaier and Roberts, 1995a,b). While a true free surface is difficult to model, a free-slip condition (i.e. assuming zero shear stress at an undeformable spherical boundary) is a much better approximation than a no-slip condition for the surface of gas- and ice-giant planets or stellar convection zones. Rigid boundaries are associated with viscous (Ekman) boundary layers, which have a damping influence on the development of strong axisymmetric flows that are found in free surface flows. Kuang and Bloxham (1997, 1999) argued that even for the geodynamo a free-slip condition may be a better choice, because the Ekman layers in the models are much thicker than the very thin layers in the Earth’s core. Aubert et al. (2001) demonstrated in rotating liquid Gallium experiments that at small Prandtl numbers – the ratio of kinematic viscosity to thermal diffusivity – flows with rigid boundaries show features similar to those with free-slip boundaries, i.e. dominant zonal flows. Miyagoshi et al. (2010) also found strong zonal flows in low Ekman number ( $\approx 10^{-7}$ ) rigid boundary geodynamo simulations. Hence, studies of dynamos with free-slip boundaries have wide ranging applications. Following these arguments, researchers have modeled Uranus’ and Neptune’s multipolar magnetic field (Stanley and Bloxham, 2004, 2006), Mercury’s weak magnetic field (Stanley et al., 2005), and Saturn’s unusually axisymmetric magnetic field (Stanley, 2010) using free-slip boundaries.

Dynamos with free-slip boundaries also exhibit bista-

Email address: yadav@mps.mpg.de (Rakesh K. Yadav)

bility: the morphology of the dynamo generated magnetic field depends on the initial magnetic field configuration (Simitev and Busse, 2009, 2012; Sasaki et al., 2011; Schrinner et al., 2012; Gastine et al., 2012). Grote and coworkers (Grote et al., 1999; Grote and Busse, 2000; Grote et al., 2000) have employed free-slip boundaries in their dynamo models, and found a wider spectrum of magnetic field geometries than what has been reported for rigid boundaries.

A direct comparison of the effects of different mechanical boundary conditions on the dynamo has rarely been made. Christensen et al. (1999) reported results for both kinds of boundary conditions for a limited number of cases and found that the large scale magnetic field is similar for both cases. Recently, Schrinner et al. (2012) have analyzed many dynamo simulations with rigid, free-slip and mixed (rigid at inner and free-slip at outer boundary) boundary conditions and report a difference in magnetic field amplitude of dipolar and multipolar dynamos. Following this study, we specifically focus here on deriving scaling properties for heat transport, velocity, and magnetic field strength. We compare our findings with earlier rigid boundary systems for which extensive modeling results are available in a broad range of control parameters (CA6). This exercise helps us in isolating the effect of mechanical boundary condition.

## 2. Dynamo model

### 2.1. MHD equations

Our numerical set-up consists of a spherical shell which rotates along the  $\hat{z}$ -axis and which is bounded by inner radius  $r_i$  and outer radius  $r_o$ . The aspect ratio  $r_i/r_o$  is 0.35. A linear variation of gravity with radius is assumed. Following previous parameter studies, we non-dimensionalize the magnetohydrodynamic (MHD) equations by using the shell thickness  $r_o - r_i = D$  as the reference length scale and  $D^2/\nu$ , where  $\nu$  is the fluid viscosity, as the time unit. The magnetic field  $\mathbf{B}$  is scaled by  $\sqrt{\rho\mu\lambda\Omega}$ , where  $\rho$  is the constant fluid density,  $\mu$  is the magnetic permeability,  $\lambda$  is the magnetic diffusivity, and  $\Omega$  is the rotation rate. The temporal evolution of velocity  $\mathbf{u}$ , temperature  $T$ , and magnetic field  $\mathbf{B}$  is governed by the MHD equations under the Boussinesq approximation

$$E \left( \frac{\partial \mathbf{u}}{\partial t} + \mathbf{u} \cdot \nabla \mathbf{u} - \nabla^2 \mathbf{u} \right) + 2\hat{z} \times \mathbf{u} + \nabla P = Ra' \frac{\mathbf{r}T}{r_o} + \frac{1}{Pm} (\nabla \times \mathbf{B}) \times \mathbf{B}, \quad (1)$$

$$\frac{\partial T}{\partial t} + \mathbf{u} \cdot \nabla T = \frac{1}{Pr} \nabla^2 T, \quad (2)$$

$$\frac{\partial \mathbf{B}}{\partial t} = \nabla \times (\mathbf{u} \times \mathbf{B}) + \frac{1}{Pm} \nabla^2 \mathbf{B}, \quad (3)$$

$$\nabla \cdot \mathbf{u} = 0, \quad (4)$$

$$\nabla \cdot \mathbf{B} = 0. \quad (5)$$

This system of equations is governed by several nondimensional control-parameters: Ekman number  $E = \nu/\Omega d^2$ ; the modified Rayleigh number  $Ra' = \alpha g_o \Delta TD / \nu \Omega$ , where  $g_o$  is

gravity at the outer boundary and  $\alpha$  is the thermal expansivity; magnetic Prandtl number  $Pm = \nu/\lambda$ ; Prandtl number  $Pr = \nu/\kappa$ ,  $\kappa$  being the thermal conductivity.  $Ra'$  is related to the conventional Rayleigh number  $Ra$  through  $Ra' = Ra E / Pr$

We assume free-slip mechanical boundaries at both inner and outer radius. The magnetic field matches a potential field at both boundaries. A fixed temperature contrast  $\Delta T$  is maintained between the top and the bottom.

### 2.2. Numerical method

Equations (1-5) are numerically solved using the MagIC code (Wicht, 2002). Velocity and magnetic field are first separated into toroidal and poloidal components as

$$\begin{aligned} \mathbf{u} &= \nabla \times u_T \hat{r} + \nabla \times \nabla \times u_P \hat{r}, \\ \mathbf{B} &= \nabla \times B_T \hat{r} + \nabla \times \nabla \times B_P \hat{r}. \end{aligned}$$

The scalar potentials  $u_{T,P}$  and  $B_{T,P}$ , along with temperature  $T$  and pressure  $P$ , are further expanded using spherical harmonics in the  $\theta$  and  $\phi$  directions and the Chebyshev polynomials in the radial direction.  $N_r$  and  $l_{max}$  are the maximum degree of the Chebyshev polynomials and the spherical harmonic functions used in this expansion. For all the simulations considered here,  $41 \leq N_r \leq 73$  and  $64 \leq l_{max} \leq 170$ . The simulations are run for at least one magnetic diffusion time ( $D^2/\eta$ ) to ensure a statistically stationary state.

### 2.3. Diagnostic parameters

We employ several diagnostic parameters to quantify the model results in terms of spatially and temporally averaged values. The Rossby number  $Ro$  quantifies the mean velocity  $u$  and is defined by  $Ro = u/(D\Omega)$ . Following CA6, we also introduce the local Rossby number  $Ro_l$  which is a more appropriate measure than  $Ro$  to characterize the ratio of the inertial and the Coriolis forces. A typical flow length scale can be calculated based on the mean spherical harmonic degree  $l$

$$\bar{l}_u = \sum_l l \langle \mathbf{u}_l \cdot \mathbf{u}_l \rangle,$$

where  $\langle \dots \rangle$  denote time average and  $\mathbf{u}_l$  is velocity component at degree  $l$ .  $Ro_l$  is then defined as  $Ro_l = Ro \pi / \bar{l}_u$ .

The mean magnetic field strength is often expressed by the Elsasser number  $\Lambda = B_{rms}^2 / \sqrt{\rho\mu\lambda\Omega}$ . However, for ease of comparison with CA6, we use the Lorentz number  $Lo = \sqrt{E\Lambda/Pm}$  to quantify the magnetic field strength. The field geometry at the outer boundary surface is characterized by its dipolarity  $f_{dip}$ . It is the ratio of the magnetic energy of the dipole to the total magnetic energy at the outer boundary surface.

The Nusselt number  $Nu$  is a ratio of total heat transported from the inner shell to the outer shell to the conducted heat. It is expected that different diffusivities play a minimal role in determining the large scale properties of the dynamo systems. This motivated CA6 to use the ‘diffusionless’ parameters  $Ro$  and  $Lo$  and also to define a modified Nusselt number  $Nu^*$  which does not involve  $\kappa$ .  $Nu^*$  is related to the conventional Nusselt number  $Nu$  via  $Nu^* = (Nu - 1)E/Pr$ . In addition, the heat flux from surfaces of astrophysical objects is a much more meaningful and

accessible quantity than the temperature difference between the inner and outer boundary of the convection zone. CA6 defined a heat flux based Rayleigh number  $Ra_Q^*$  which incorporates the advected heat flux rather than the temperature contrast.  $Ra_Q^*$  is related to  $Ra$  through  $Ra_Q^* = Ra(Nu - 1)E^3/Pr^2$ .

### 3. Results

We have built up a data set of 57 dynamo simulations with free-slip boundaries: 40 cases by us (see Table A.2) and 17 cases adopted from Schrinner et al. (2012). All of the cases in this data set have the same physical set-up as described above. Also, following CA6, we report and analyze only those dynamo simulations which have  $Nu > 2$  to ensure a vigorous enough convection that fills the full volume of the spherical shell.

#### 3.1. Bistability

Bistability is a phenomenon in which a system shows two different dynamo solutions, i.e. dipolar and multipolar, for the same set of control parameters, but with different initial conditions for the magnetic field. For dynamos with free-slip boundaries, Simitev and Busse (2009) found two distinct dipolar and multipolar dynamo branches, at least in some parameter range. Recently, Sasaki et al. (2011), Schrinner et al. (2012), and Gastein et al. (2012) have also observed bistability in their dynamo simulations with free-slip boundaries. Such bistable branches have rarely been observed in dynamos with rigid boundaries, e.g. CA6 reported a single case in which they found bistable states.

We plot in Fig. 1 the dipolarity  $f_{dip}$  at the outer surface ( $r = r_o$ ) versus the local Rossby number  $Ro_l$  (for our simulations). In the dipolar branch (filled data points) the magnetic field is dominated by the dipole ( $f_{dip} > 0.4$ ) and in the multipolar branch (empty data points) the dipole is much weaker ( $f_{dip} < 0.05$ ). The dipole branch is limited to cases with  $Ro_l \lesssim 0.2$ . However, the multipolar branch exists for a broad range of  $Ro_l$ . The highly supercritical dipolar case at  $Ro_l \approx 0.2$  ( $E = 1 \times 10^{-4}$ ,  $Pm = 0.5$  and  $Ra' = 4000$ ) was run for two magnetic diffusion times without an indication of a dipole collapse, although we can not exclude that the field could change to multipolar in long run. Dipolar dynamo at such high  $Ro_l$  has not been reported yet. Simulations that settle down to different dynamo states depending on the initial magnetic field are marked with a “+” in Fig. 1 (difficult to discern on the multipolar branch due of clustering). Note that other dipolar dynamos could show bistability but we did not explore all of our dipolar cases for such behavior.

For rigid boundary dynamos, CA6 reported that multipolar dynamo solutions are not observed for  $Ro_l < 0.1$ . But results from Schrinner et al. (2012) and our findings suggest that this is not the case for free-slip boundaries. We also found few dynamo solutions, which have  $Ro_l < 0.1$ , but settle to a multipolar solution despite having initial dipolar magnetic field. For example, we only found a multipolar solution for  $E = 3 \times 10^{-4}$  and  $Pm \leq 1.5$ . This demonstrates that, depending on the control parameters, only the multipolar dynamo branch can be stable

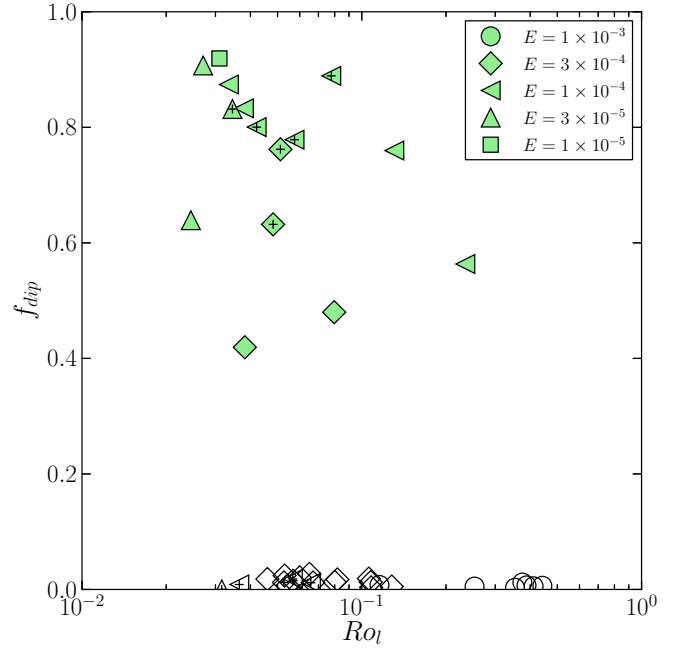


Figure 1: Dipolarity at the outer boundary versus the local Rossby number. The data points carrying “+” marker are bistable states. Filled (empty) symbols are dipolar (multipolar) dynamos. The symbol shapes represent the Ekman number and the corresponding value is given in the upper-right-corner box.

in some situations. This is in agreement with earlier results (Simitev and Busse, 2009, 2012) which showed that bistability is in-fact a function of  $P$ ,  $Pm$  and  $E$ . They used volumetric heating while we use a fixed temperature contrast to drive convection. The bistable behavior we observed generalizes their findings.

One of the characteristic features of rotating spherical shell convection with free-slip boundaries is the development of strong axisymmetric zonal flows. In rigid boundary systems, the Reynolds stresses, which arise due to a statistical correlation between the radial and azimuthal flow component (in cylindrical co-ordinates), are balanced by the bulk viscosity and the Ekman layer friction near the outer boundary. In case of free-slip boundaries, the Ekman layers are absent and zonal flows can thus saturate at much higher vigour. In dynamo models, Maxwell stresses also affect the zonal flows; these stresses are potentially higher in dipolar dynamos that have higher magnetic field strength than multipolar ones at the same control parameter values (Browning, 2008). One argument for the essential role of zonal flows for bistability is that an initial dipolar magnetic field inhibits the growth of zonal flows via Maxwell stresses. In case of a multipolar initial condition, strong zonal flows can develop, which in turn suppress the development of dipolar magnetic fields. This mechanism allows multipolar magnetic fields even for  $Ro_l$  smaller than 0.1. The resulting zonal flow structure of a bistable state is shown in Fig. 2. It portrays a weak thermal-wind driven zonal flow in the dipolar case

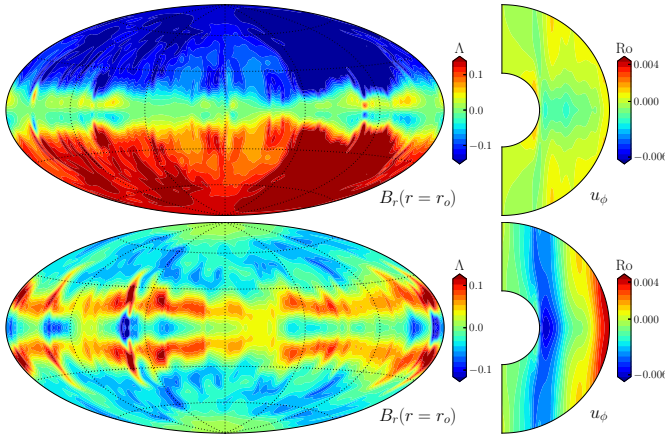


Figure 2: Non dimensional radial magnetic field at outer boundary and zonal flow (azimuthally averaged) in a meridional section for a dipolar (top row) and a multipolar (bottom row) dynamo. These states are obtained at  $E = 3 \times 10^{-5}$ ,  $Pm = 0.5$ , and  $Ra' = 900$ . The radial magnetic field is truncated at 50% of the maximum in order to highlight the magnetic field structures.

and a nearly three times stronger geostrophic zonal flow in the multipolar case. The non-geostrophy of the flow in case of the dipolar dynamo emphasizes that the Lorentz force is actively participating in the force balance of the dynamo mechanism, while this is not the case in the multipolar dynamo. As also pointed out before by Schrinner et al. (2012).

### 3.2. Nusselt number scaling

Figure 3 shows that the modified Nusselt number  $Nu^*$  scales very well with the flux-based Rayleigh number  $Ra_Q^*$  in the same way irrespective of whether the dynamo is dipolar (filled symbols) or multipolar (empty symbols). A best-fit line to this data set reveals a relation  $Nu^* = 0.061 Ra_Q^{*0.52}$ , which agrees well with the scaling  $Nu^* = 0.076 Ra_Q^{*0.53}$  (dashed line) found by CA6 for dipolar dynamos with rigid boundaries. For convection in rotating shells without magnetic field, Christensen (2002) suggested a possible asymptotic scaling  $Nu^* = 0.077 Ra_Q^{*5/9}$  in the limiting case of  $E \rightarrow 0$ . All these scaling relations are very close to each other, which suggests that neither the magnetic field nor the mechanical boundary conditions have substantial effect on the scaling behavior of heat transport in rotating spherical shell convection. However, we note that for larger values of the Rossby number than the ones considered here, in a regime where inertia dominates over the Coriolis force, the power-law scaling between  $Nu^*$  and  $Ra_Q^*$  breaks down (Schmitz and Tilgner, 2010; King et al., 2010).

### 3.3. Rossby number scaling

In Fig. 4 we plot  $Ro$  as a function of  $Ra_Q^*$ . The data points are slightly more scattered as compared to Fig. 3, but a consistent scaling is nonetheless evident. Moreover, a somewhat different scaling for dipolar and multipolar dynamos is visible as demonstrated by the two different solid lines. These lines are  $Ro = 0.73 Ra_Q^{*0.39}$  (dipolar) and  $Ro = 1.78 Ra_Q^{*0.44}$  (multipolar). The scaling reported by CA6 for dipolar rigid boundary

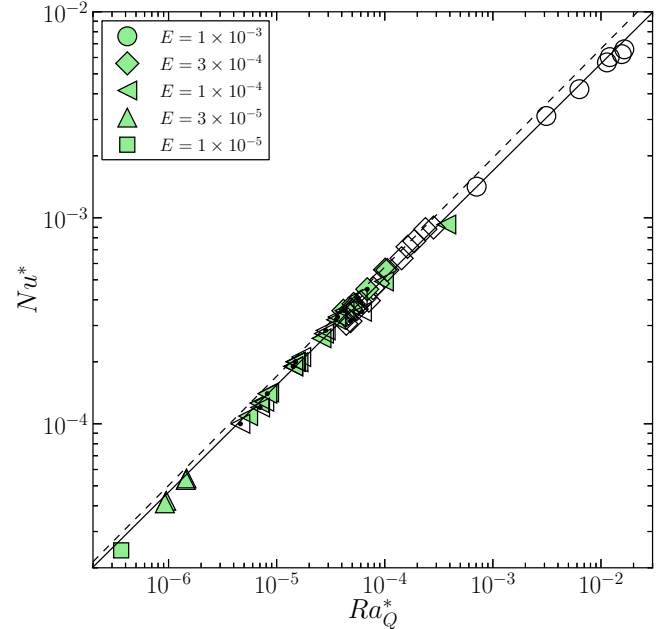


Figure 3: Modified Nusselt number versus heat flux based Rayleigh number. The data symbols carrying a thick black dot are adopted from Schrinner et al. (2012). The solid-line is a line-fit to data and the dashed-line is the scaling reported by CA6 for dipolar rigid boundary dynamos.

dynamics is  $Ro = 0.85 Ra_Q^{*0.41}$  (dashed-line), which agrees with our dipolar dynamo scaling.

Similar to CA6, the scatter in Fig. 4 can be reduced to some extent by assuming an additional  $Pm$  dependence. A two-parameter least-square-optimized fit provides  $Ro = 0.99 Ra_Q^{*0.41} Pm^{-0.1}$  (dipolar) and  $Ro = 2.44 Ra_Q^{*0.47} Pm^{-0.14}$  (multipolar). This optimization reduces the standard error by 48% in the dipolar scaling and 20% in the multipolar scaling (see Table 1). We also considered the Ekman number as additional parameter for improving the fit, but, as observed by CA6, the resulting exponents are rather small as compared to  $Ro$  and  $Pm$  exponents. Hence, we discard a dependence on  $E$  in our scaling analysis. The  $Pm$  exponent is small and appears to depend on the nature of the magnetic field. The latter could be an artifact of relatively small size of the data set, especially for dipolar dynamos. In fact, similar to CA6, assuming a scaling of the form  $Ro \propto (Ra_Q^* Pm^{-1/3})^\alpha$ , a good fit is obtained for both dipolar and multipolar cases, with somewhat different values for  $\alpha$  (see Table 1). This simplified form is shown in Fig. 5.

As described in Sec. 3.1, zonal flows are stronger in rotating convective shells with free-slip mechanical boundaries. In the corresponding MHD systems, dynamos with multipolar magnetic fields will have stronger zonal flows as compared to those with dipolar magnetic fields. This effect is visible in Fig. 6 whose top panel shows  $Ro_{\text{non-zonal}}$  versus  $Ra_Q^*$ , and the bottom panel shows  $Ro_{\text{zonal}}$  versus  $Ra_Q^*$ .  $Ro_{\text{non-zonal}}$  and  $Ro_{\text{zonal}}$  are calculated by considering the rms velocity exclud-

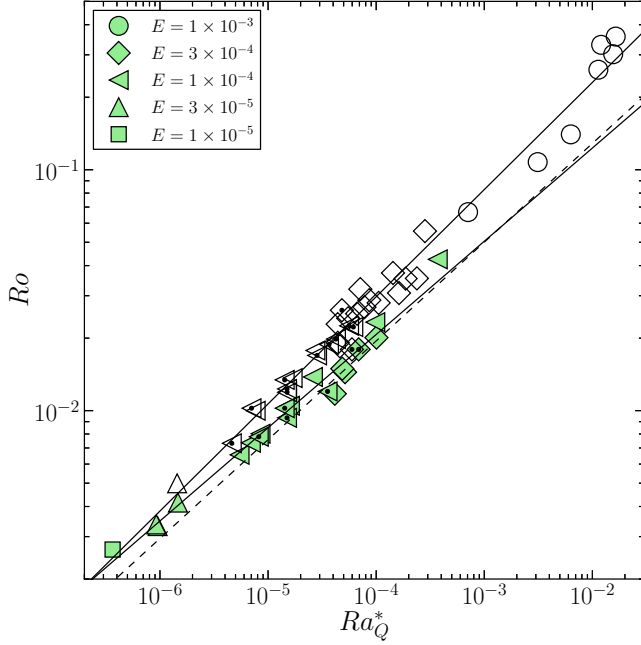


Figure 4: Rossby number versus the heat flux based Rayleigh number. The two solid lines are best-fitting lines to dipolar and multipolar dynamos. The dashed-line represent the scaling reported by CA6 for dipolar rigid boundary dynamos.

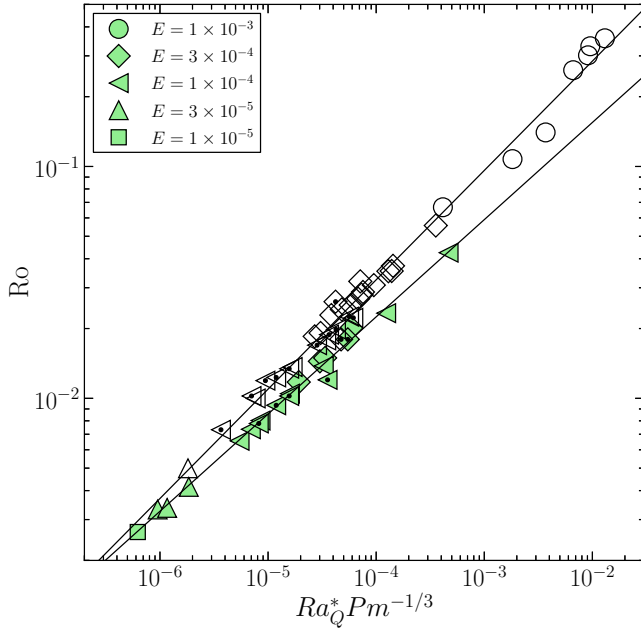


Figure 5: A simplified form of Rossby number scaling incorporating a  $Pm$  dependence.

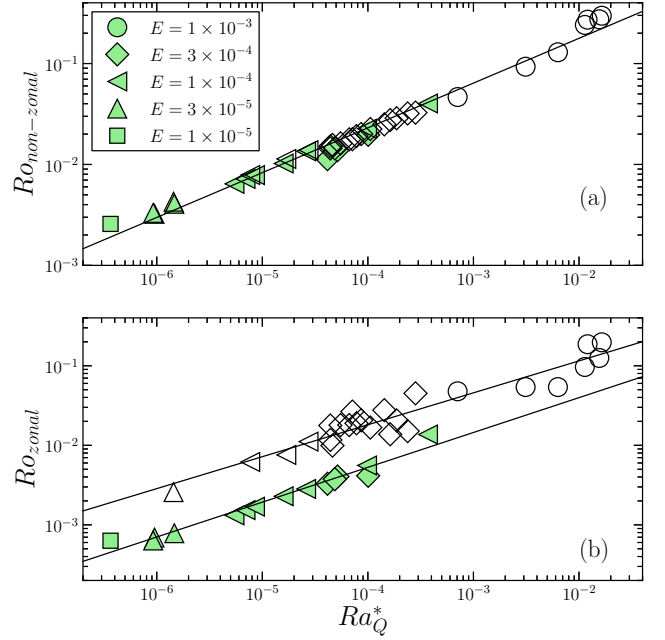


Figure 6: Non-zonal Rossby number in (a) and zonal Rossby number in (b) versus the heat flux based Rayleigh number.

ing the axisymmetric zonal-flow component and the rms velocity of only the axisymmetric zonal flow, respectively. The scaling in Fig. 6a is  $Ro_{non-zonal} = 1.37 Ra_Q^{*0.44}$  and in Fig. 6b is  $Ro_{zonal} = 0.29 Ra_Q^{*0.44}$  (dipolar) and  $Ro_{zonal} = 0.73 Ra_Q^{*0.4}$  (multipolar). The zonal Rossby number of dipolar dynamos is consistently lower than that of corresponding multipolar dynamos, while the non-zonal Rossby number is almost unaffected by the field topology. This difference in zonal flows explains the offset in the Rossby number scaling in dipolar and multipolar dynamos seen in Fig. 4 and 5. Note that as compared to the dipolar branch the scatter in the multipolar branch of Fig. 6b is large. This could be due to the fact that unlike the dipolar branch the multipolar branch is a blend of dynamos which have quadrupolar, octopolar, and sometimes even higher order modes as the most dominating magnetic mode. Since the Maxwell stresses are dependent on the magnetic field geometry, the zonal flows saturate at many different levels.

### 3.4. Magnetic field scaling

The Ohmic dissipation time  $\tau_{mag}$ , which is the ratio of magnetic energy and Ohmic dissipation, is a function of the typical length scale of the magnetic field. As the magnetic Reynolds number is increased, the magnetic field becomes smaller scaled, and, since small scales are associated with faster time scales, the Ohmic dissipation time scale decreases. This qualitative argument was verified by Christensen and Tilgner (2004) in rigid boundary spherical shell dynamos. They showed that  $\tau_{mag}$  (normalized with magnetic diffusion time) is approximately inversely proportional to the magnetic Reynolds number  $Rm$ .

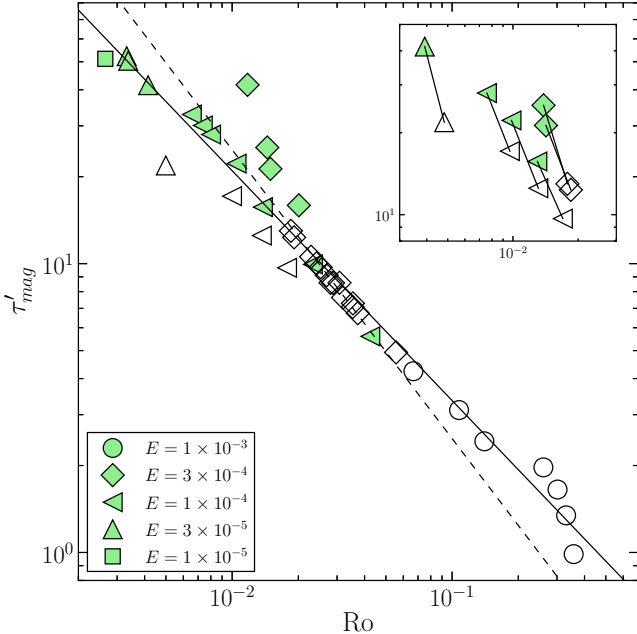


Figure 7: Ohmic dissipation time versus the Rossby number. Solid line represents a best fit line, while the dashed line represents  $\tau'_{mag} \propto 1/Ro$ . The inset figure contains bistable pairs connected by solid lines.

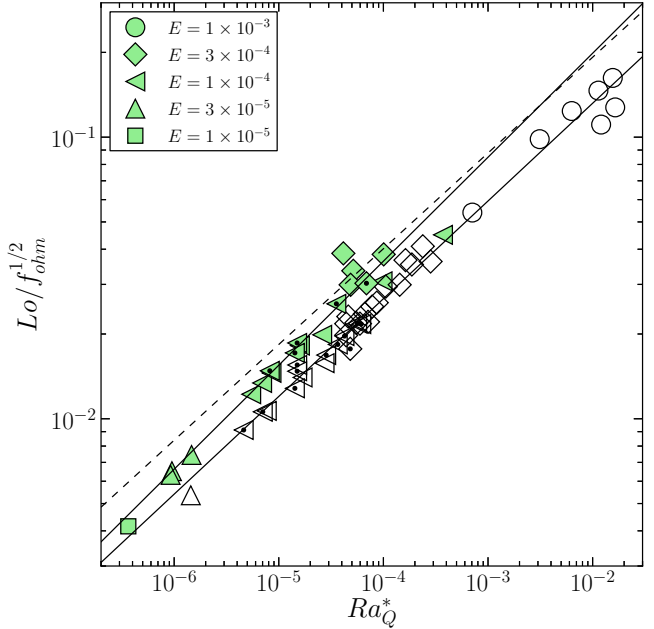


Figure 8: Corrected Lorentz number versus the heat flux based Rayleigh number. The two solid lines are best-fitting lines to dipolar and multipolar dynamos. The dashed-line represent the scaling reported by CA6 for dipolar rigid boundary dynamos.

When  $\tau'_{mag}$  is the Ohmic dissipation time expressed in units of rotation period of the spherical shell, this inverse relation translates to  $\tau'_{mag} \propto 1/Ro$ . In Fig. 7 we plot  $\tau'_{mag}$  versus  $Ro$ . A best-fit line to this data set suggests  $\tau'_{mag} \propto 1/Ro^{0.8}$ . Since the scatter in Fig. 7 is substantial, the difference between the exponents -0.8 and -1 may not be very significant. Christensen (2010) have discussed a more complex scaling for  $\tau_{mag}$  and report a marginal improvement in the quality of the fit. Although the inset figure shows a small decrease in  $\tau'_{mag}$  for bistable states when the magnetic field is multipolar, the scalings for dipolar and multipolar dynamos appears to follow the same trend. Moreover, if we plot  $\tau'_{mag}$  versus  $Ro_{\text{zonal}}$  or  $Ro_{\text{non-zonal}}$  (not shown), then the scatter is increased as compared to Fig. 7. It highlights that the important parameter in the context of ohmic dissipation is the *total* Rossby number, which incorporates the zonal-flow contribution.

CA6 argue that the magnetic field strength might be determined by the power available to balance the Ohmic dissipation. Following this argument, the Lorentz number should be accordingly corrected by the Ohmic fraction  $f_{ohm}$  which is the ratio of Ohmic dissipation and the power generated via buoyancy forces. In Fig. 8, we plot the corrected Lorentz number  $Lo/f_{ohm}^{1/2}$  versus the flux-based Rayleigh number  $Ra_Q^*$ , which is a non-dimensional measure for the power generated by the action of buoyancy forces (CA6). A best fit is obtained by  $Lo/f_{ohm}^{1/2} = 1.09 Ra_Q^{*0.37}$  (dipolar) and  $Lo/f_{ohm}^{1/2} = 0.65 Ra_Q^{*0.35}$  (multipolar). The dipolar scaling in Fig. 8 is close to the rigid boundary dipolar scaling  $Lo/f_{ohm}^{1/2} = 0.92 Ra_Q^{*0.34}$  (dashed

line) reported by CA6. Furthermore, a two-parameter optimized fit for dipolar dynamos is  $Lo/f_{ohm}^{1/2} = 0.72 Ra_Q^{*0.33} Pm^{0.14}$  and for multipolar dynamos is  $Lo/f_{ohm}^{1/2} = 0.51 Ra_Q^{*0.33} Pm^{0.11}$ . The inclusion of  $Pm$  reduces the standard error by 67% (dipolar) and 39% (multipolar). Again, assuming a simplified form  $Lo/f_{ohm}^{1/2} \propto (Ra_Q^* Pm^{1/3})^\beta$ , the quality of the fit is hardly reduced (Table 1, Fig. 9). A cursory inspection of Figs. 8 and 9 suggests that the dipolar and multipolar scalings are almost the same except for an offset in the pre-factor by  $\approx 8/5$ .

An inverse relation of  $\tau'_{mag}$  and  $Ro$  translates to  $Lo/f_{ohm}^{1/2} \propto \sqrt{Ra_Q^*/Ro}$ . If we now substitute the  $Ro$  scaling from Fig. 4 in the previous relation, then an offset of  $\approx 8/5$  is indeed expected for dipolar and multipolar scaling. The  $\tau'_{mag} \propto 1/Ro$  argument therefore supports the offset in the scaling observed in Fig. 8 to a good extent. Schrinner et al. (2012) have also reported similar shift in the  $Lo/f_{ohm}^{1/2}$  scaling. They, however, qualitatively argue that the offset in the scaling is due to decrease in the  $f_{ohm}$  in multipolar dynamo cases. More analysis is required to conclusively demonstrate the reason for such an offset.

#### 4. Discussion and conclusions

In this article we investigated the effect of free-slip mechanical boundaries on various scaling laws in spherical shell dynamos. We compared the inferred scaling laws with earlier reported scalings for rigid boundary dynamos.

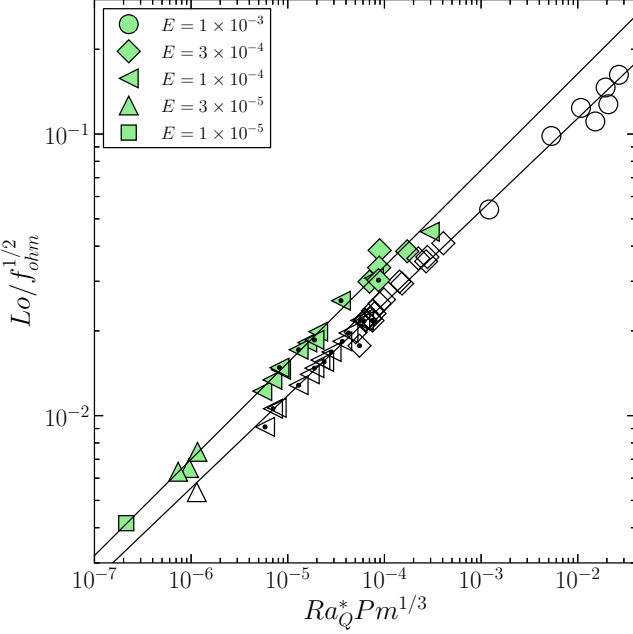


Figure 9: A simplified form of corrected Lorentz number scaling incorporating a  $Pm$  dependence.

Table 1: The various scaling laws inferred from our study, along with the cross-correlation coefficient  $R$  and the Standard error (standard deviation divided by square-root of number of data points).

	$R$	Standard-error
$Nu^* = 0.061 Ra_Q^{*0.52}$	0.9987	0.0036
$Ro_{non-zonal} = 1.37 Ra_Q^{*0.44}$	0.9924	0.0089
Dipolar		
$Ro = 0.73 Ra_Q^{*0.39}$	0.9903	0.0128
$Ro_{zonal} = 0.29 Ra_Q^{*0.44}$	0.9840	0.0219
$Ro = 0.99 Ra_Q^{*0.41} Pm^{-0.1}$	0.9976	0.0067
$Ro = 1.07 (Ra_Q^* Pm^{-1/3})^{0.42}$	0.9966	0.0082
$Lo/f_{ohm}^{1/2} = 1.09 Ra_Q^{*0.37}$	0.9819	0.0168
$Lo/f_{ohm}^{1/2} = 0.72 Ra_Q^{*0.33} Pm^{0.14}$	0.9972	0.0056
$Lo/f_{ohm}^{1/2} = 0.79 (Ra_Q^* Pm^{1/3})^{0.34}$	0.9967	0.0066
Multipolar		
$Ro = 1.78 Ra_Q^{*0.44}$	0.9916	0.0098
$Ro_{zonal} = 0.73 Ra_Q^{*0.4}$	0.9553	0.0259
$Ro = 2.44 Ra_Q^{*0.47} Pm^{-0.14}$	0.9954	0.0078
$Ro = 2.49 (Ra_Q^* Pm^{-1/3})^{0.47}$	0.9952	0.0078
$Lo/f_{ohm}^{1/2} = 0.65 Ra_Q^{*0.35}$	0.9941	0.0064
$Lo/f_{ohm}^{1/2} = 0.51 Ra_Q^{*0.33} Pm^{0.11}$	0.9975	0.0039
$Lo/f_{ohm}^{1/2} = 0.52 (Ra_Q^* Pm^{1/3})^{0.33}$	0.9975	0.0039

We observed bistability, i.e. dipolar and multipolar dynamos coexisting for same control parameters. This agrees with the earlier findings (Simev and Busse, 2009, 2012; Sasaki et al., 2011; Schrinner et al., 2012; Gastine et al., 2012) and reinforces the importance of free-slip boundaries and zonal flows for this phenomenon.

The modified Nusselt number scales as  $Nu^* = 0.061 Ra_Q^{*0.52}$  which is in very close agreement with the scaling for rigid boundary dynamos (Christensen and Aubert, 2006) and non-magnetic convection in spherical shell with free-slip boundaries (Christensen, 2002). This highlights that boundary conditions or magnetic field do not effect the scaling behavior of heat-transport in convective spherical shells.

The Rossby number scales as  $Ro = 0.73 Ra_Q^{*0.39}$  for dipolar and as  $Ro = 1.78 Ra_Q^{*0.44}$  for multipolar dynamos. The offset in the scaling of dipolar and multipolar dynamos can be attributed to different zonal flow characteristics: zonal flow quenching is stronger in a dipolar magnetic field configuration as compared to a multipolar configuration. This results in a smaller pre-factor in the Rossby number scaling for dipolar dynamos.

The corrected Lorentz number scales as  $Lo/f_{ohm}^{1/2} = 1.09 Ra_Q^{*0.37}$  for dipolar dynamos and  $Lo/f_{ohm}^{1/2} = 0.65 Ra_Q^{*0.35}$  for multipolar dynamos. The exponents are almost identical but the pre-factors differ. We investigated the origin of such shifted scaling and found that, using the scaling for Rossby number (inferred from our data-set) and an inverse relationship between ohmic dissipation time and magnetic Reynolds number, parallel and shifted scalings for  $Lo/f_{ohm}^{1/2}$  are indeed expected. The observed and the expected ratio of dipolar and multipolar  $Lo/f_{ohm}^{1/2}$  scalings were in good agreement.

Similar to Christensen and Tilgner (2004) and Christensen and Aubert (2006), we also observed that a small dependence on the magnetic Prandtl number improves the quality of the scalings, especially in the dipolar dynamo cases. However, results from the Karlsruhe laboratory dynamo experiment motivated Christensen and Tilgner (2004) to conjecture that such small  $Pm$  dependence might disappear when  $Pm \ll 1$ . The lowest  $Pm$  in our study is of order unity, which makes it difficult to ascertain this conjecture. So far, our free-slip simulations and the rigid boundary simulation results of Christensen and Aubert (2006) support scalings which have some  $Pm$  contribution. Simulations which attain  $Pm \ll 1$  will shed more light on this issue.

Christensen et al. (2009) showed that the scaling derived from Boussinesq dynamo simulations with rigid boundaries can predict the magnetic field strength in rapidly rotating stars. Objects such as stars and giant planets have free-surface flows, very high density stratification, and probably fully convective interiors. Similar scaling of physical properties despite such drastic physical differences is puzzling. Our analysis shows that the boundary conditions do not substantially effect the scaling behavior of the rms velocity and the magnetic field strength, which supports the observations of Christensen et al. (2009). Future simulations of dynamos with density stratification and fully convective interiors will address the remaining critical factors.

## Acknowledgements

We are grateful to Martin Schrinner for providing extra information about his free-slip dynamo simulations. RKY and TG acknowledge financial support from the SFB 963 and the special priority program 1488 (PlanetMag, <http://www.planetmag.de>) of the DFG respectively. All the figures were generated using *matplotlib* ([www matplotlib org](http://www matplotlib org)).

## References

Aubert, J., Brito, D., Nataf, H.C., Cardin, P., Masson, J.P., 2001. A systematic experimental study of rapidly rotating spherical convection in water and liquid gallium. *Phys. Earth Planet. Int.* 128, 51–74.

Aubert, J., Labrosse, S., Poitou, C., 2009. Modelling the palaeo-evolution of the geodynamo. *Geophys. J. Int.* 179, 1414–1428.

Browning, M.K., 2008. Simulations of dynamo action in fully convective stars. *Astrophys. J.* 676, 1262–1280.

Christensen, U., Olson, P., Glatzmaier, G.A., 1999. Numerical modelling of the geodynamo: a systematic parameter study. *Geophys. J. Int.* 138, 393–409.

Christensen, U.R., 2002. Zonal flow driven by strongly supercritical convection in rotating spherical shells. *J. Fluid Mech.* 470, 115–133.

Christensen, U.R., 2010. Dynamo scaling laws and applications to the planets. *Space Sci. Rev.* 152, 565–590.

Christensen, U.R., Aubert, J., 2006. Scaling properties of convection-driven dynamos in rotating spherical shells and application to planetary magnetic fields. *Geophys. J. Int.* 166, 97–114.

Christensen, U.R., Holzwarth, V., Reiners, A., 2009. Energy flux determines magnetic field strength of planets and stars. *Nature* 457, 167.

Christensen, U.R., Tilgner, A., 2004. Power requirement of the geodynamo from ohmic losses in numerical and laboratory dynamos. *Nature* 429, 169–171.

Gastine, T., Duarte, L., Wicht, J., 2012. Dipolar versus multipolar dynamos: the influence of the background density stratification. *Astronomy & Astrophysics* 546, A19.

Glatzmaier, G.A., Roberts, P.H., 1995a. A three-dimensional convective dynamo solution with rotating and finitely conducting inner core and mantle. *Phys. Earth Planet. Int.* 91, 63–75.

Glatzmaier, G.A., Roberts, P.H., 1995b. A three dimensional self consistent computer simulation of a geomagnetic field reversal. *Nature* 377, 203–209.

Grote, E., Busse, F.H., 2000. Hemispherical dynamos generated by convection in rotating spherical shells. *Physical Review E* 62, 4457–4460.

Grote, E., Busse, F.H., Tilgner, A., 1999. Convection-driven quadrupolar dynamos in rotating spherical shells. *Physical Review E* 60, R5025–8.

Grote, E., Busse, F.H., Tilgner, A., 2000. Regular and chaotic spherical dynamos. *Phys. Earth Planet. Int.* 117, 259–272.

Jones, C.A., 2011. Planetary magnetic fields and fluid dynamos. *Annual Rev. of Fluid Mech.* 43, 583–614.

Kageyama, A., Sato, T., 1995. Computer simulation of a magnetohydrodynamic dynamo. II. *Phys. of Plasmas* 2, 1421.

King, E.M., Soderlund, K.M., Christensen, U.R., Wicht, J., Aurnou, J.M., 2010. Convective heat transfer in planetary dynamo models. *Geochem. Geophys. Geosys.* 11, 1–19.

Kuang, W., Bloxham, J., 1997. An Earth-like numerical dynamo model. *Nature* 389, 371–374.

Kuang, W., Bloxham, J., 1999. Numerical modeling of magnetohydrodynamic convection in a rapidly rotating spherical shell: weak and strong field dynamo action. *J. Comput. Phys.* 153, 51–81.

Miyagoshi, T., Kageyama, A., Sato, T., 2010. Zonal flow formation in the Earth's core. *Nature* 463, 793–6.

Olson, P., Christensen, U.R., 2006. Dipole moment scaling for convection-driven planetary dynamos. *Earth and Planet. Sci. Lett.* 250, 561 – 571.

Sasaki, Y., Takehiro, S.i., Kuramoto, K., Hayashi, Y.Y., 2011. Weak-field dynamo emerging in a rotating spherical shell with stress-free top and no-slip bottom boundaries. *Phys. Earth Planet. Int.* 188, 203–213.

Schmitz, S., Tilgner, A., 2010. Transitions in turbulent rotating rayleigh-bénard convection. *Geophys. Astrophys. Fluid Dyn.* 104, 481–489.

Schrinner, M., Petitdemange, L., Dormy, E., 2012. Dipole collapse and dynamo waves in global direct numerical simulations. *The Astrophysical Journal* 752, 121.

Simitev, R.D., Busse, F.H., 2009. Bistability and hysteresis of dipolar dynamos generated by turbulent convection in rotating spherical shells. *Europhys. Lett.* 85, 19001.

Simitev, R.D., Busse, F.H., 2012. Bistable attractors in a model of convection-driven spherical dynamos. *Physica Scripta* 86, 018409.

Stanley, S., 2010. A dynamo model for axisymmetrizing Saturn's magnetic field. *Geophys. Res. Lett.* 37, L05201.

Stanley, S., Bloxham, J., 2004. Convective-region geometry as the cause of Uranus and Neptunes unusual magnetic fields. *Nature* 428, 151–153.

Stanley, S., Bloxham, J., 2006. Numerical dynamo models of Uranus' and Neptune's magnetic fields. *Icarus* 184, 556–572.

Stanley, S., Bloxham, J., Hutchison, W.E., Zuber, M.T., 2005. Thin shell dynamo models consistent with Mercurys weak observed magnetic field. *Earth and Planet. Sci. Lett.* 234, 27 – 38.

Takahashi, F., Matsushima, M., Honkura, Y., 2008. Scale variability in convection-driven MHD dynamos at low Ekman number. *Phys. Earth Planet. Int.* 167, 168–178.

Wicht, J., 2002. Inner-core conductivity in numerical dynamo simulations. *Phys. Earth Planet. Int.* 132, 281–302.

## Appendix A. Simulation data

Table A.2: Simulations results. The Prandtl number  $Pr$  is unity. The  $Pm$  values of bistable multipolar dynamos are marked with “\*”.

$E$	$Pm$	$Ra'$	$Nu$	$Rm$	$Ro_l$	$Ro_{zonal}$	$\Lambda$	$f_{dip}$	$f_{ohm}$
$1 \times 10^{-3}$	5	500	2.42	322.14	0.116	0.0477	2.21	0.0078	0.15
	5	1000	4.12	515.39	0.253	0.0540	10.31	0.005	0.21
	5	1500	5.21	701.42	0.353	0.0540	18.18	0.003	0.24
	5	2000	6.68	1223.29	0.375	0.0966	27.71	0.012	0.26
	5	2500	7.23	1412.75	0.411	0.1253	33.55	0.0055	0.25
	2	2000	7.03	635.74	0.388	0.1866	0.72	0.007	0.029
	2	2500	7.57	685.70	0.442	0.1971	2.17	0.0064	0.067
$3 \times 10^{-4}$	10	510	2.18	376.64	0.0382	0.0033	30.42	0.419	0.61
	5	450	2.27	230.73	0.048	0.0041	10.64	0.632	0.57
	5*	450	2.14	297.35	0.057	0.0099	2.19	0.051	0.17
	5	600	2.86	324.21	0.080	0.0041	11.68	0.48	0.48
	5	750	3.41	489.15	0.108	0.0138	6.87	0.0036	0.31
	5	900	3.94	562.90	0.128	0.0151	9.45	0.005	0.34
	3	450	2.20	142.04	0.051	0.0037	4.50	0.762	0.5
	3*	450	2.09	185.08	0.053	0.0117	1.07	0.012	0.22
	3	630	2.86	270.97	0.080	0.0167	2.43	0.013	0.28
	3	810	3.57	335.20	0.108	0.0206	3.90	0.0127	0.31
	1.5	480	2.02	110.82	0.046	0.0177	0.37	0.018	0.19
	1.5	510	2.20	116.79	0.053	0.0179	0.51	0.024	0.21
	1.5	540	2.37	121.74	0.060	0.0180	0.65	0.021	0.23
	1.5	570	2.52	129.47	0.065	0.0189	0.76	0.027	0.24
	1.5	600	2.60	138.66	0.067	0.0206	0.82	0.012	0.25
	1	600	2.50	95.72	0.062	0.0226	0.46	0.0059	0.2
	1	750	3.12	119.29	0.081	0.0275	0.81	0.0103	0.27
	0.5	1050	3.99	89.35	0.106	0.0451	0.53	0.0188	0.24
$1 \times 10^{-4}$	1	500	2.09	62.39	0.034	0.0013	0.63	0.8741	0.42
	1	550	2.26	69.76	0.038	0.0015	0.77	0.8329	0.43
	1	600	2.42	75.82	0.042	0.0017	0.92	0.8004	0.43
	1*	600	2.28	96.8	0.0365	0.0062	0.33	0.0086	0.29
	1	800	2.99	98.48	0.058	0.0023	1.51	0.7786	0.46
	1*	800	3.11	130.97	0.057	0.0075	0.63	0.018	0.32
	0.5	1000	3.6	64.81	0.078	0.0028	0.80	0.8891	0.4
	0.5*	1000	3.74	84.98	0.066	0.011	0.43	0.0111	0.34
	0.5	2000	5.91	109.98	0.131	0.0056	2.20	0.7598	0.46
	0.5	4000	10.28	203.61	0.234	0.0137	4.31	0.563	0.43
$3 \times 10^{-5}$	1	750	2.41	104.84	0.025	0.0007	0.70	0.6392	0.49
	0.5	750	2.37	53.38	0.027	0.0006	0.26	0.2583	0.39
	0.5	900	2.81	65.25	0.035	0.0008	0.37	0.8711	0.4
	0.5*	900	2.78	80.3	0.032	0.0026	0.15	0.0001	0.32
$1 \times 10^{-5}$	0.2	1500	3.43	50.05	0.031	0.0006	0.11	0.92	0.32